Demonstrating the Use of a Fungal Synthesized Quinone in a Redox Flow Battery

Wilhelmsen, Charlotte Overgaard; Kristensen, Sebastian Birkedal; Nolte, Oliver; Volodin, Ivan A.; Christiansen, Johan Vormsborg; Isbrandt, Thomas; Sørensen, Trine; Petersen, Celine; Sondergaard, Teis Esben; Lehmann Nielsen, Kåre

Total number of authors:
16

Published in:
Batteries and Supercaps

Link to article, DOI:
10.1002/batt.202200365

Publication date:
2023

Document Version
Publisher's PDF, also known as Version of record

Research Article
doi.org/10.1002/batt.202200365

Chemistry Europe
European Chemical Societies Publishing

www.batteries-supercaps.org

Demonstrating the Use of a Fungal Synthesized Quinone in a Redox Flow Battery

Charlotte Overgaard Wilhelmsen,*[a] Sebastian Birkedal Kristensen,[a] Oliver Nolte,[b] Ivan A. Volodin,[b] Johan Vormsborg Christiansen,[c] Thomas Isbrandt,[c] Trine Sørensen,[d] Celine Petersen,[d] Teis Esben Sondergaard,[d] Kåre Lehmann Nielsen,[d] Thomas Ostenfeld Larsen,[c] Jens Christian Frisvad,[c] Martin D. Hager,[b] Ulrich S. Schubert,[b] Jens Muff,*[a] and Jens Laurids Sørensen*[a]

Aqueous organic redox flow batteries (AORFBs) have gained increased interest as a promising solution to store energy from sustainable energy sources. Inspired by naturally occurring bio-quinones, we here propose a new electrolyte based on the fungal compound phoenicin. Phoenicin was produced using the filamentous fungus *Penicillium atrosanguineum* at a concentration of 1.24 g L^{-1} liquid medium and extracted using ethyl acetate to a purity exceeding 95%. The fungus may provide a benefit of high scalability of the biosynthesis-based production of the electroactive substance. Here, we demonstrate the performance of biologically produced phoenicin as a negative electrolyte in an RFB against ferro/ferricyanide, as a proof of concept, giving an initial capacity of 11.75 Ah L^{-1} and a capacity decay of 2.85% day^{-1}. For a deeper investigation of the battery setup, *in situ* attenuated total reflection infrared (ATR-IR) spectra of the phoenicin electrolyte were recorded. Symmetric cell cycling was performed to study the stability of this bio-based active material.

Introduction

The development of renewable energy technologies is important to meet the increasing worldwide electricity demand in a sustainable manner.[1,2] To utilize the full potential of renewables, their intermittent nature needs to be taken into account. The need for cost-effective stationary energy storage devices is critical to balance supply and demand within the electricity grid. In redox flow batteries (RFBs), electricity is stored by changing the redox state of redox-active species dissolved in recirculating liquid electrolytes. These electrolytes are stored in external tanks separated from the electrochemical cell[3–8] (Figure 1), providing independent scalability of both power and energy output that makes RFBs a unique and flexible storage technology.[4,9–12] RFBs with various redox chemistries and solvents have been proposed, with the currently most advanced systems being based on vanadium ions as electrolyte material. However, vanadium RFBs are restricted by the abundance of vanadium ores, the large CO2 footprint as well as a strong dependency on commodity prices,[5,13–15] with the current system capital cost about two to five times above the target of 100 $ kWh^{-1} (recommended by US Department of Energy).[16,17] Addressing this, there has been an increasing interest in aqueous organic redox flow batteries (AORFBs) within the last decade, which offer new opportunities for the design and construction of sustainable batteries.[18] As opposed to vanadium-based RFB systems, AORFBs employ electrolytes based on organic redox-active species from earth-abundant elements.[19] Among the most well-investigated compounds for AORFBs are quinones, which includes systems using anthraquinones,[20–24] benzoquinones,[5,25,26] and naphtoquinones,[27,28] viologens,[29–32] TEMPO-based (2,2,6,6-tetramethylpiperidine-1-oxyl) organic radicals,[33–36] and ferrocenes,[6,37] as well as others.[38–41] The high interest in quinones as active materials in RFB electrolytes is based on both their ability to feature reversible two-electron redox reactions[42] and their structural diversity. Moreover, a fine-tuning of parameters, such as the electrochemical potential or

[a] C. O. Wilhelmsen, Dr. S. B. Kristensen, Dr. J. Muff, Dr. J. L. Sørensen
Department of Chemistry and Bioscience, Section of Chemical Engineering
Aalborg University
Niels Bohrs Vej 8, 6700 Esbjerg, Denmark
E-mail: cowi@bio.aau.dk
jm@bio.aau.dk
jls@bio.aau.dk
[b] O. Nolte, I. A. Volodin, Dr. M. D. Hager, Prof. U. S. Schubert
Laboratory of Organic and Macromolecular Chemistry (IOMC) and Center for Energy and Environmental Chemistry Jena (CEEC Jena)
Friedrich Schiller University of Jena
Humboldtstrasse 10 (IOMC) and Philosophenweg 7a (CEEC Jena), 07743 Jena, Germany
[c] J. V. Christiansen, Dr. T. Isbrandt, Prof. T. O. Larsen, Prof. J. C. Frisvad
Department of Biotechnology and Biomedicine
Technical University of Denmark
Søltofts Plads Building 221, 2800 Kongens Lyngby, Denmark
[d] T. Sørensen, C. Petersen, Dr. T. E. Sondergaard, Prof. K. Lehmann Nielsen
Department of Chemistry and Bioscience, Section of Biotechnology
Aalborg University
Fredrik Bajers Vej 7H, 9220 Aalborg Ø, Denmark

Supporting information for this article is available on the WWW under https://doi.org/10.1002/batt.202200365

Research Article
doi.org/10.1002/batt.202200365
Chemistry Europe
European Chemical Societies Publishing

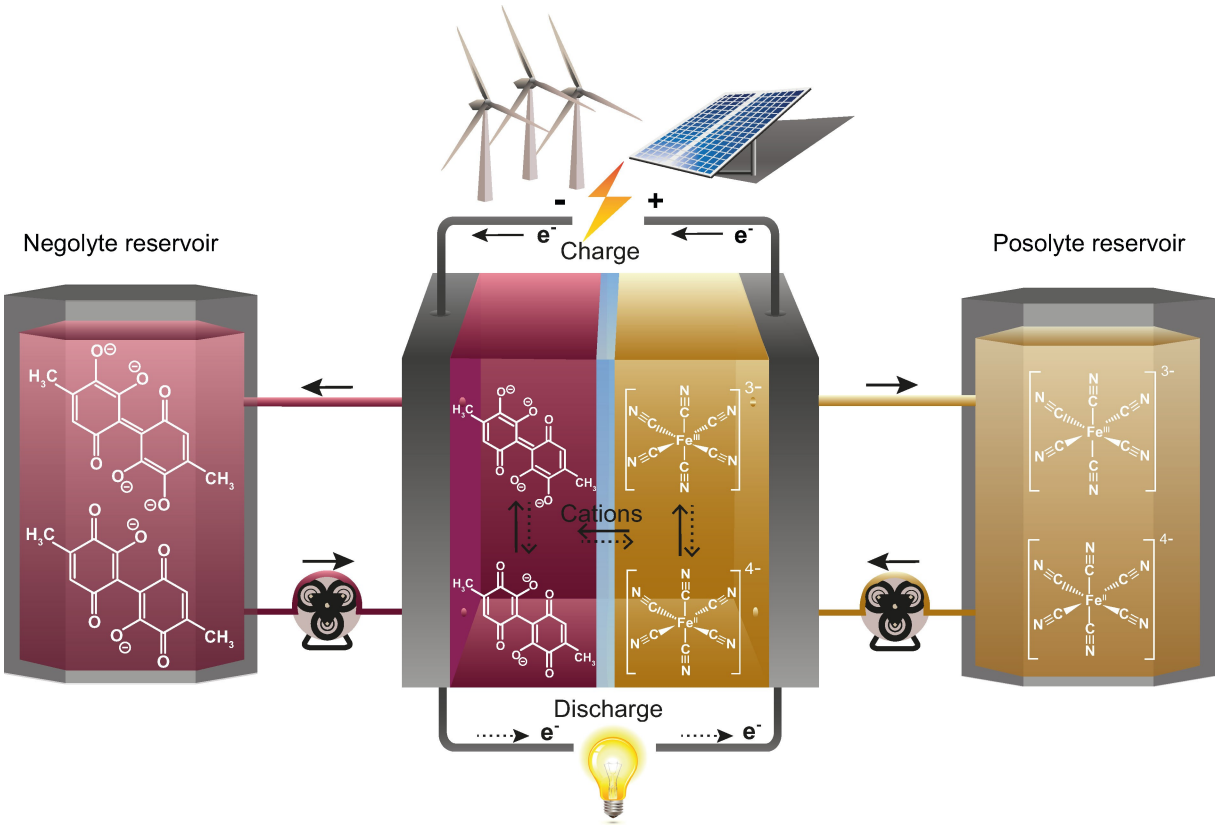

Figure 1. Schematic representation of the fungal RFB. The two half cells of the RFB contain phoenicin as negolyte (red) and potassium ferro/ferricyanide as posolyte (yellow), which are separated by a cation exchange membrane (blue), preventing the mixture of the electrolytes and electroactive species and allowing transport of potassium cations. Solid and dashed arrows indicate the transport of electrons and cations upon the charging and discharging processes of the RFB, respectively. Additionally, solid arrows indicate the direction of the electrolyte flow.

the compound's solubility, can be adjusted by the introduction of different functional groups to the quinoid core.[5,43]

While almost all quinones tested in RFBs so far have been synthetically prepared from non-renewable feedstock, a redox-active material based on lignin as raw material for further synthetic modifications was recently proposed[44] as a step towards using renewable feedstocks. Nonetheless, to ensure low-cost, high availability, and low environmental impact of the employed compounds, more research is required on bio-produced quinones from renewable feedstocks.[38,44,45] In nature, quinones not only occur within plants but are also common in living organisms such as bacteria and fungi. They contribute to biochemical and physiological functions with their ability to undergo reversible redox reactions.[46–48] Biosynthetic approaches to manufacture desired chemical compounds are commonly used, in particular in the production of pharmaceutical agents.[49] Furthermore, new approaches such as synthetic biology, aiming at the use of organisms to specifically produce desired agents have been investigated as well.[50]

However, to the best of our knowledge, biosynthetic quinones have not been considered for use in an RFB electrolyte. Within this contribution, we, therefore, investigate the use of a fungal compound, phoenicin (see Figure 1 on the left side), as the redox-active material for an aqueous RFB. Based on a systematic screening and simulation of electrochemical properties of naturally occurring quinones,[51] we identified phoenicin as one of the potential candidates to be applied as a negolyte electroactive substance in RFBs. Phoenicin was synthesized biologically from *Penicillium atrosanguineum*, giving an extract with a concentration of 1.24 g L^{-1} and a purity exceeding 95%. Subsequent electrochemical characterization of the biosynthetic phoenicin was performed, and an investigation of its performance in an alkaline AORFB electrolyte in a symmetric flow battery revealed phoenicin being most stable when held in its reduced form rather than its oxidized form. A full RFB test with phoenicin as a negolyte paired against potassium ferro/ferricyanide was performed. The cell exhibited a theoretical operating voltage of 0.86 V and a theoretical and practical capacity of 10.7 Ah L^{-1} and 11.75 Ah L^{-1} respectively at a concentration of 0.2 M of phoenicin as an electroactive substance and 2.1 M of KOH as a supporting electrolyte, demonstrating the potential of the presented approach. Results of the test are represented by a capacity decay rate of 2.85% day^{-1} (over ~14 days) and 0.35% $cycle^{-1}$ (over 119 cycles), and a coulombic efficiency of 98.5%. The electrochemical findings are further supported by *in-situ* ATR-IR measurements implemented in the full cell setup.

Research Article
doi.org/10.1002/batt.202200365
Chemistry Europe
European Chemical Societies Publishing

Results and Discussion

Biosynthesis of phoenicin.

Phoenicin (Figure S1a) was firstly isolated in 1933 from Penicillium phoeniceum.[52] Subsequently, the chemical synthesis[53,54] and biosynthesis[55] of the compound have been investigated, and it has recently been shown that Penicillium species can produce phoenicin in amounts of up to 4.9 g L^{-1}.[56] Phoenicin is structurally similar to oosporein, which has an extra hydroxyl group, positioned at the vacant carbon atom in each of the two quinoid rings (Figure S1). The biosynthetic gene cluster for oosporein has previously been identified in Beauveria bassiana,[57] and consequently, based on this finding the putative phoenicin gene cluster in P. atrosanguineum was identified (Figure S2a). The phoenicin gene cluster was predicted to consist of a polyketide synthase (PhS1), a transcription factor (PhS3), a hydroxylase (PhS4), and a laccase (PhS5), which are all present as orthologous in the oosporein gene cluster. The involvement of the gene cluster in phoenicin biosynthesis was further validated by disrupting PhS1 by a CRISPR (clustered regularly interspaced short palindromic repeats)/Cas9 approach (Figure S2b), which consequently abolished phoenicin production in the resulting transformant (Figure S2c). We therefore propose that phoenicin biosynthesis follows a similar path as oosporein, starting with biosynthesis of orsellinic acid by PhS1, which is then simultaneously decarboxylated and hydroxylated (PhS4) and dimerized (PhS5) to phoenicin (Figure S2d).

The workflow for the production of phoenicin is shown in Figure 2. Within the presented study, *Penicillium atrosanguineum* was used to produce phoenicin. Fungal cultures of fungal spore suspension were added to Czaoek-yeast-broth growth media and incubated for 14 days at 25 °C in darkness following the procedure described in the methods section. The dark red/violet supernatant from incubated cultivations of the fungus was extracted and refined with a three-step liquid:liquid partitioning and from one liter medium, we extracted 1.24 g of 95 % pure phoenicin. The extract was identified by tandem MS (Figure S3) as well as by ^{1}H and ^{13}C NMR (Figure S4), and the purity analysis can be seen in Figures S5 and S6. After the extract was freeze-dried and the purity of the resulting phoenicin was determined, phoenicin was dissolved in the supportive electrolyte to be exploited as the negolyte in an RFB.

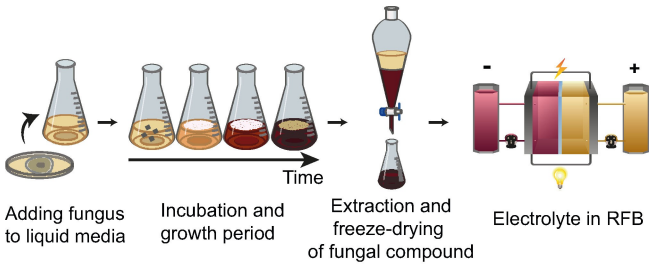

Figure 2. Workflow towards the fungal battery. Schematic representation of the workflow for the production of the redox-active fungal compound phoenicin, which afterward can be directly used to prepare the RFB electrolyte.

Phoenicin is an intensely red-colored compound consisting of two covalently bound benzoquinone cores (Figure 3). Due to the acidity of the hydroxyl groups ($pK_{a1} = 3.02$, $pK_{a2} = 5.95$),[58] the diquinone can be deprotonated in an alkaline solution. A subsequent electrochemical two-electron reduction yields a tetra-anionic molecule as seen in Figure 3.

Electrochemical characterization

As Figure 4(a) shows, a high pH alkaline solution (1 M KOH) of phoenicin has a half-wave potential of −0.37 V *vs.* SHE. When varying the scan rate (Figure 4c), the dependence of the peak

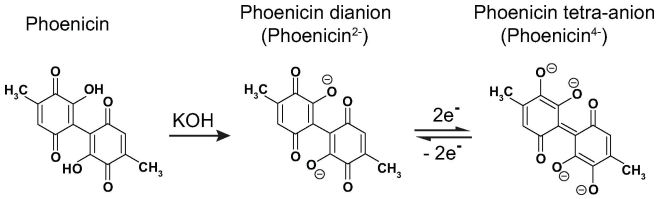

Figure 3. Schematic representation of the proposed redox mechanism of phoenicin in high alkaline solution. Deprotonation of phoenicin in 1 M KOH yields the dianion phoenicin^{2-}. An electrochemical reduction of phoenicin^{2-} in an alkaline solution produces a phoenicin tetra-anion (phoenicin^{4-}). This reaction is assumed to occur in the battery when phoenicin is used as a negolyte in 1 M KOH. During the battery charge, the reduced form of phoenicin^{4-} is produced, and during the discharge, the oxidized phoenicin^{2-} form is generated.

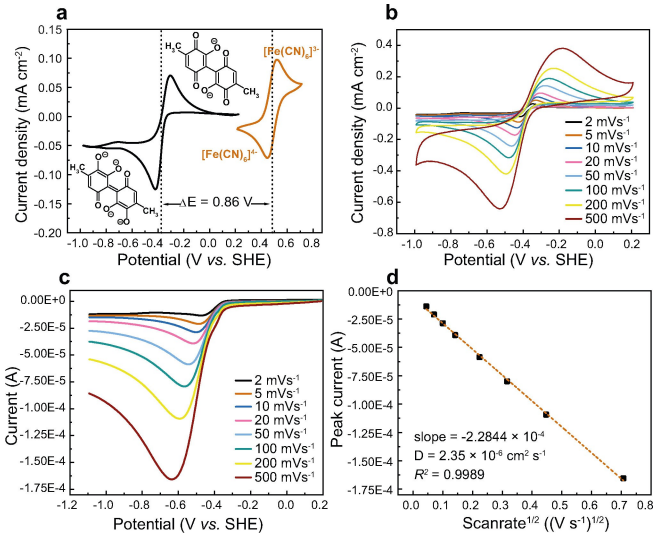

Figure 4. Voltammetric analysis of phoenicin. a) Voltammograms of 1.0×10^{-3} M phoenicin and 1.0×10^{-3} M ferrocyanide dissolved in 1 M KOH using a scan rate of 10 mV s^{-1}. For the voltammetric investigations a glassy carbon disk working electrode, an Ag/AgCl reference electrode, and a platinum wire counter electrode were used. b) Voltammograms of 1.0×10^{-3} M phoenicin dissolved in 1 M KOH at different scan rates. c) Randles-Sevcik analysis of cathodic currents of 3.0×10^{-3} M phoenicin in 1 M KOH at different scan rates using linear sweep voltammetry. d) Plot of cathodic peak current vs. square root of scan rate. Peak currents were obtained from the Randles-Sevcik analysis.

Research Article
doi.org/10.1002/batt.202200365
Chemistry Europe
European Chemical Societies Publishing

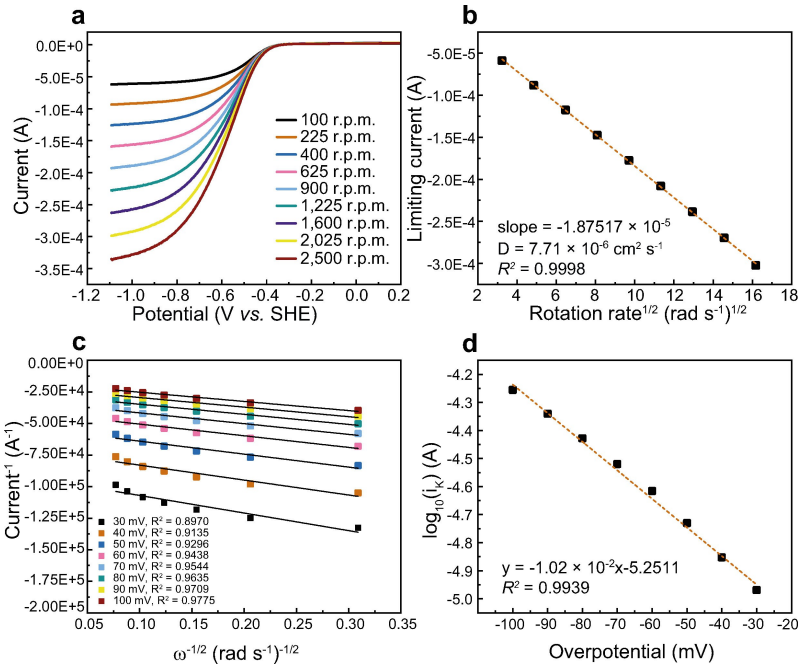

Figure 5. Rotating disc electrode measurements of phoenicin. a) Current *vs.* potential at selected rotation rates using a potential sweep rate of 5 mV s^{-1}, for the reduction of 3.0×10^{-3} M phoenicin in 1 M KOH. For the RDE investigations, a rotating glassy carbon disk (3 mm diameter) working electrode, an Ag/AgCl reference electrode, and a platinum wire counter electrode were used. b) Plot of limiting current vs. square root of rotation rate (Levich plot). The limiting currents were an average of the currents between −0.78 and −0.88.1 V *vs.* SHE. c) Koutecky-Levich plot of different overpotentials (deviation from the reduction potential of −0.37 V *vs.* SHE). d) Kinetically limiting current (adapted from Koutecky-Levich plot) vs. overpotential (Tafel plot).

current on the square root of the scan rate shows strong linearity, as evidenced by the large R^2 value (Figure 4d), and the increase of cathodic and anodic peak splits, which follows the increase in potential sweep rate (Figure 4b) indicates the electrochemically quasi-reversible nature of the redox reaction of phoenicin.[59]

The diffusion coefficient is among the main factors, determining how fast the mass transport of the active species towards the electrode in the battery is. Thus, to ensure the potential of the RFB cell to reach high power output, considering convection and migration parameters to be fixed, a high diffusion coefficient is preferable. The diffusion coefficient of phoenicin was obtained from the Randles-Sevcik analysis and rotating disc electrode (RDE) measurements. To detect the real concentration of phoenicin in the electrochemical analysis, an absorbance-calibration curve was made using UV-vis (Figure S7). A UV-vis spectrum of the phoenicin solution was taken before and after the Randles-Sevcik analysis, and the resulting average concentration was found to be 2.76×10^{-3}±1.6×10^{-4} M phoenicin in 1 M KOH (see Table S1, and Figure S8). From the slope obtained in the peak current versus the square root of the scan rate plot (Figure 4d), the diffusion coefficient was determined to be 2.35×10^{-6} cm^2 s^{-1}.

A UV-vis spectrum of the phoenicin solution was also taken before and after the RDE experiment, and the resulting average concentration was found to be 2.64×10^{-3}±2.5×10^{-4} M phoenicin in 1 M KOH (Table S1 and Figure S9a). By analysis of the Koutecky-Levich plot of limiting current versus square root of rotation rate (Figure 5b) from the RDE measurements, the diffusion coefficient was determined to be 7.71×10^{-6} cm^2 s^{-1}, which is larger than the one obtained from the Randles-Sevcik analysis.

Still, these diffusion coefficients are comparable to the values, determined from the RDE experiments, for other quinones studied as RFB electrolytes (Table 1).

From the slope of the Tafel plot (Figure 5d), the transfer coefficient (α) was determined to be 0.60 and from the intercept, the electron transfer rate constant (k^0) was calculated to be 1.56×10^{-4} cm s^{-1}. This is faster than k^0 of DMBQ but still 10 times slower than the electron transfer rate constants for DHBQ and 2,3-HCNQ (Table 1), which corresponds to a quasi-reversible behavior of the redox reaction of phoenicin, and consequently, agrees with the results from the cyclic voltammetry experiment. In 1 M KOH, phoenicin shows a solubility of

Table 1. Comparison of the diffusion coefficient and electron transfer rate constant of different compounds used in redox flow batteries. All values are determined from the RDE experiments and a glassy carbon electrode was used in all cases.

Compound	D [cm^2 s^{-1}][a]	k^0 [cm s^{-1}][b]	Solubility [M]	Ref.
Phoenicin	7.71×10^{-6}	1.56×10^{-4}	0.4	This work
DMBQ[d]	3.42×10^{-6}	7.70×10^{-5}	–	[3]
DHBQ[e]	3.66×10^{-6}	2.12×10^{-3}	4	[5]
2,3-HCNQ[f]	3.44×10^{-6}	2.07×10^{-3}	1.2	[43]

[a] Diffusion coefficient. [b] Electron transfer rate constant. [c] Working electrode material. [d] 2,5-Dimethyl-3,6-dihydroxy-,4-benzoquinone. [e] 2,5-Dihydroxy-1,4-benzoquinone. [f] 2-Hydroxy-3-carboxy-1,4-napthoquinone.

Research Article
doi.org/10.1002/batt.202200365
Chemistry Europe
European Chemical Societies Publishing

0.4 M determined by UV-vis (Figure S10), which is lower compared to the ones for DHBQ[5] and 2,3-HCNQ,[43] both measured in 1 M KOH, seen in Table 1.

Symmetric cell cycling.

Organic redox-active species are prone to capacity losses by various means. Sources for capacity loss among organic compounds include crossover, electrolyte leakage, reaction with oxygen as well as degradation reactions.[60] The utilization in grid-scale applications, however, requires a stable capacity over long periods for the battery electrolytes to ensure the economical viability of the system. Therefore, methods to distinguish between the different sources of capacity loss have been developed, as recently summarized.[61] The currently most well-established electrochemical method to analyze the overall influence of molecular capacity loss mechanisms in AORFBs is represented by the volumetrically unbalanced, compositionally symmetric flow cell cycling method.[62]

To study the capacity retention of phoenicin using the symmetric cycling method, a pre-charged electrolyte at 50% state of charge (SOC) was split into two unequal volumes, resulting in one reservoir having a capacity-limiting effect (Figure 6a). This allows for the operator to theoretically access the full SOC range of the capacity limiting side (CLS). Additionally, as both CLS and non-capacity limiting side (NCLS) contain electrolytes with identical composition, the influence of reactant crossover between the battery half-cells is significantly reduced.

Potentiostatic cell cycling with potential limits of ±300 mV (Figure S11a) revealed an initial capacity decay of 13.6% day^{-1} (Table S2). The cycling was paused at different SOCs of the CLS for 24 hours, followed by 10 charge/discharge cycles after each pause. According to the capacity loss, estimated between the pauses, phoenicin is more stable in its reduced form (high SOC) with a decay of 4.1% day^{-1} (Figure 6b), while when it is kept in oxidized form (low SOC), the capacity loss reaches 18.0% day^{-1}. This observation of capacity loss measured in this experiment indicates that the decay in the battery capacity is SOC-dependent or, in other words, it depends on the concentration of the oxidized and reduced forms of phoenicin. Paying attention to the sequence where the electrolyte was paused at 50-100-95-90% SOC, the average capacity loss is considerably lower when compared to the pauses at 0-5-10% SOC (Figure 6b). Here, a reversal in behavior can be seen when the concentration of the reduced form of phoenicin exceeds the concentration of the oxidized form of phoenicin. This is supported by the structural stability of phoenicin in its reduced and oxidized form, as discussed before. The capacity loss can be considered unrelated to electrochemical side reactions, as the cell is not cycled during the pauses and is thus assumed to be purely chemical. Furthermore, side reactions with oxygen as well as reactant crossover can be neglected due to the employed experimental setup. No leakages were observed. Phoenicin being most stable in its reduced form is opposite to the behavior seen for other quinones such as 2,6-dihydroxy anthraquinone (DHAQ)[62] and 2,3-HCNQ,[43] which both are more stable than the oxidized form with a decay of 0.1% day^{-1} and 0.6% day^{-1} respectively. In contrast, phoenicin appears more stable when being kept in its reduced form compared to the DHAQ and 2,3-HCNQ, which showed a decay of 18.0% day^{-1} and 14.4% day^{-1} respectively.

On a molecular level, a reaction with the strongly alkaline supporting electrolyte is the most probable explanation for the capacity loss of phoenicin, as this has already been observed for other structurally related quinones.[5,63] As Figure S12 shows, phoenicin comprises an unsubstituted carbon atom that can be electronically activated due to its β-position to a ketone moiety, acting as a Michael acceptor for nucleophiles such as OH^-. We, therefore, propose the mechanism seen in Figure S12 as the

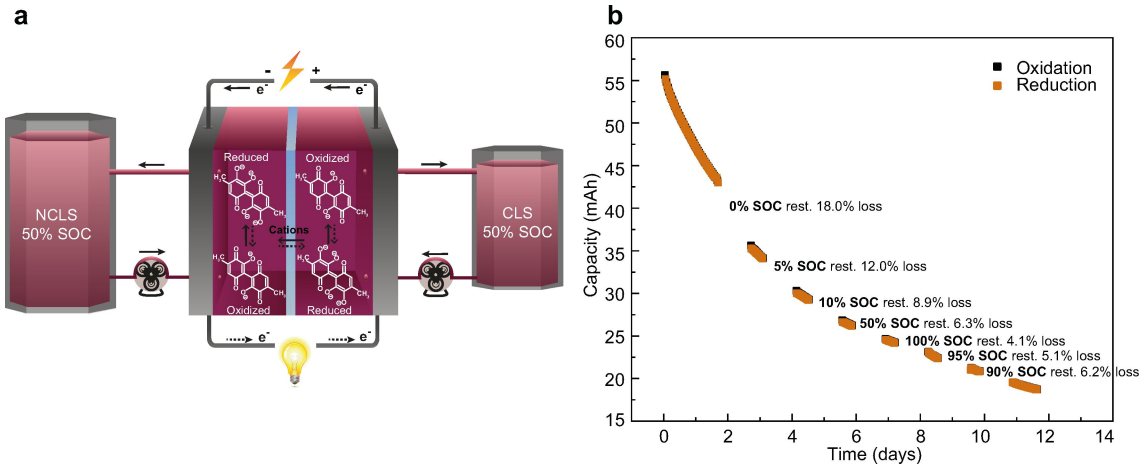

Figure 6. Volumetrically unbalanced, compositionally symmetric flow cell test of 0.1 M phoenicin. a) Schematic of the symmetric flow cell. Both reservoirs contain 50% SOC 0.1 M phoenicin. The capacity limiting side (CLS) contains 10 mL of solution, and the non-capacity limiting side (NCLS) contains 20 mL of solution. When applying a positive current, the CLS was oxidized and the NCLS was reduced. b) Capacity loss over time from the continuous cell cycling and the cycling combined with 24 h pauses at variable fixed SOCs.

Research Article
doi.org/10.1002/batt.202200365
Chemistry Europe
European Chemical Societies Publishing

hypothesis for some of the capacity loss observed in the cycling test.

Full flow battery cell cycling

The performance of phoenicin in a full-cell RFB setup was tested using a counter-half-cell comprised of ferro/ferricyanide in a nitrogen-filled glove bag. In this experiment, the negolyte contained 0.2 M phoenicin in 2.1 M KOH, while the posolyte was composed of 0.16 M $K_4Fe(CN)_6$/0.04 M $K_3Fe(CN)_6$ in 1 M KOH. With phoenicin being the limiting side, the theoretical capacity of this battery would be 10.7 Ah L^{-1} for a two-electron reaction. To ensure that the capacity loss and cycling behavior can be ascribed to the performance of the negolyte, an excess of ferrocyanide was used (stoichiometric ratio of 1.3). Initially, an open-circuit voltage of 0.87 V of the battery was measured, matching the recorded CV data.

The stability of phoenicin in a full cell was evaluated from charge-discharge cycles over approximately 14 days (119 cycles) (Figure 7a) with a coulombic efficiency average of around 98.5% and an energy efficiency of 36.9% on average. A combination of galvanostatic and potentiostatic cycling regimes (Figure S11c) resulted in an initial capacity of 11.75 Ah L^{-1} (235.1 mAh), which matches the theoretical capacity of a two-electron reaction. Throughout the experiment (14 days), the capacity dropped to 6.97 Ah L^{-1}, halving roughly every 19 days. When averaged over the entire experimental runtime, a capacity decay of 2.85% day^{-1} (0.35% $cycle^{-1}$) was observed. The loss in capacity per day (2.85% day^{-1}) is lower compared to the losses seen during cycling in the symmetric cell cycling experiment (Table S2). The initial charge and discharge cycle showed an energy density of 4.7 Wh L^{-1} and 1.74 Wh L^{-1}, respectively, taking both electrolyte volumes into account.[13]

A capacity loss of 2.85% day^{-1} (0.35% $cycle^{-1}$) is comparable with the decays presented for other quinones tested in RFBs against $K_4Fe(CN)_6$ and reported in the literature. Phoenicin has greater stability and similar coulombic efficiency compared to the DHBQ, tested in a setup using a concentration of 0.5 M and a Nafion 115 membrane, demonstrating a capacity loss of 9% day^{-1} (0.24% $cycle^{-1}$), a coulombic efficiency of 99%, and an energy density of 5.87 Wh L^{-1}.[5,60] This also accounts when we compare with another study using the 2,6-DHAQ, cycled with a concentration of 0.5 M and a Nafion 212 membrane, ensuing capacity loss of 8% day^{-1} (0.1% $cycle^{-1}$) and a coulombic efficiency of 99%.[64] Still, there are also examples of more stable quinone-based molecules, such as, e.g., the 2,6-DHAQ structure, which has further been functionalized with alkali-soluble carboxylate terminal groups to produce the 2,6-DBEAQ, performing with a capacity loss of only 0.05% day^{-1} (0.001% $cycle^{-1}$) cycled against $K_4Fe(CN)_6$.[20]

For a more detailed investigation of the performance of the phoenicin battery, in situ ATR-IR spectra of the negolyte were recorded during cycling. Therefore, the phoenicin solution was pumped from its reservoir through the ATR-IR device before entering the battery cell, providing a spectrum of the composition of the negolyte every 90 seconds. During charging, the peaks at 1064, 1204, and 1384 cm^{-1} increase, representing the reduced state, while the peaks at 1276 and 1508 cm^{-1} decrease, as they represent the oxidized state of phoenicin, as shown in Figure 7(b).

To validate the electrochemical findings, the first derivative spectra of the IR data representing a fully charged and discharged negolyte (phoenicin in its reduced and oxidized form, respectively) were used as dependent variables in a multiple linear regression (MLR) model (Figure S13). With this model, the molar fractions of both the oxidized and reduced forms of phoenicin can be deduced from the IR data as a function of time, and from here it is seen that the phoenicin electrolyte was cycled in the full SOC range from near zero to 100% SOC (Figure S13d). Interestingly, the initial SOC differs from zero (roughly 25%, Figure S13b), which may be attributed to the initial ratio of phoenicin, and its hydrogenated and dihydrogenated forms present in the starting material, as supported by HPLC-MS measurements (Figure S5).

Subsequent linear regressions for both redox species, seen in Figure S13d, show a higher linear correlation coefficient for the reduced form of phoenicin, giving a further hint that the oxidized redox state is more likely to suffer from decomposi-

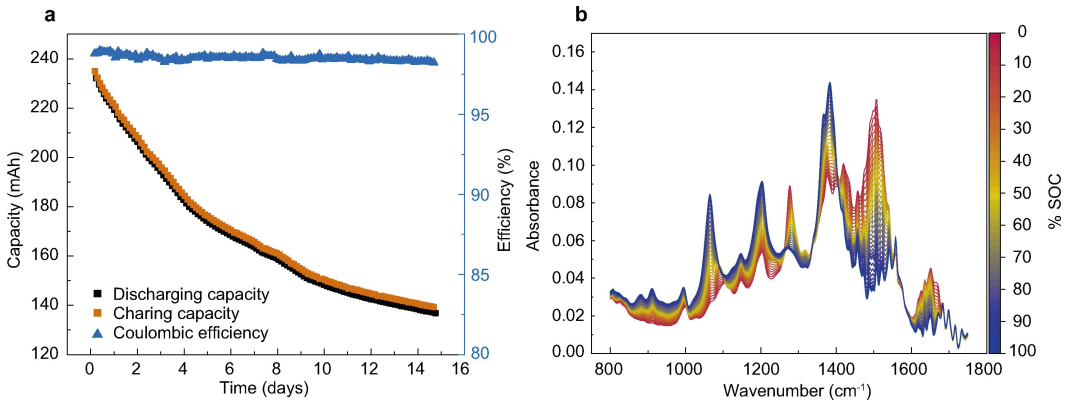

Figure 7. Full cell battery cycling. a) Capacity loss and Coulombic efficiency of the full cell composed of 0.2 M phoenicin in 20 mL 2.1 M KOH as negolyte and 0.16 M ferrocyanide/0.04 M ferricyanide in 60 mL 1 M KOH as posolyte. b) Stack-plot of one charging half-cycle of phoenicin colored by the SOC.

tion, matching the results of the symmetric cell cycling experiments.

Besides this, aging due to the degradation of phoenicin can also be seen in the raw IR data (Figure S14). When comparing spectra of both redox states of phoenicin before and after prolonged cycling, changes in both the intensity of the signals representing the respective redox states as well as in the general shape of the spectrum are visible. However, a simple assignment of additionally occurring peaks to new functional groups was not possible due to the strong influence of the negative charges yielded by deprotonation of the hydroxyl groups in the alkaline electrolyte. Nevertheless, the capacity loss seen in the full cell cycling (Figure 7a) can be linked to the phoenicin electrolyte and the degradation seen in the IR data (Figure S14d). According to the experimental data obtained, it can be assumed that the SOC of the negolyte (phoenicin) can be monitored by the ATR-IR. These assumptions are supported by the visible differences in the spectrum for the fully oxidized and reduced forms of phoenicin.

Since the initial SOC was measured to be roughly 25% (Figure S13b), it can be assumed that phoenicin decomposes or structurally reorganizes when dissolved in high alkaline KOH, which is backed up by the concentration difference measured in the voltammetric experiments from UV-vis measurements (Table S1). Therefore, it can be discussed if the starting SOC of the symmetric cell cycling experiment was 50% as assumed, or if the actual SOC after preparing the electrolyte was higher. When preparing the 50% SOC electrolyte for symmetric cell cycling, equal amounts of fully charged and uncharged phoenicin was mixed. Taking the initial SOC of 25% in the full cell cycling experiment into account, it can be questioned if the fully charged phoenicin was mixed with an equal amount of uncharged phoenicin for the symmetric cell cycling experiment, or if the SOC of the uncharged phoenicin differed from zero, resulting in a SOC above 50% after mixing. This could explain the difference in capacity loss seen in the two cycling experiments.

Conclusion

In this study, we explored the possibility to use a natural compound, namely a fungal quinoid metabolite without any further structural modifications as a charge-storage material in an aqueous-organic redox flow battery. The employed phoenicin, produced in scalable amounts by *Penicillium astrosanguineum*, was therefore extracted by a simple liquid:liquid extraction and used without further purification as redox-active material in electrochemical experiments. Volumetrically unbalanced, compositionally symmetric flow cell cycling was conducted, showing a moderate performance with a capacity fade of 13.6% day^{-1} in the initial cycles before implementation of pauses at fixed SOCs and, subsequently, with a capacity fade rate of 6.3% day^{-1} when cycled after the last pause. Along with the full experiment of 12 days duration, a loss of 66% was seen in total. Furthermore, during full-cell RFB cycling against potassium ferro/ferricyanide posolyte, the performance of the battery has shown a coulombic efficiency of 98.5% and a decay rate of 2.85% day^{-1} (0.35% $cycle^{-1}$). The full RFB cycling experiment was combined with *in situ* ATR-IR measurements in support of the electrochemical findings. Even though the performance of the presented negolyte is not on par with other high-performance quinones published recently,[20] it is still comparable to other simpler quinones.[3,5,43,64] The employed phoenicin can be seen as a model compound as it is using an environmentally benign source for the active materials. Across the fungal spectrum, more than 358 quinones have been described, which represent a huge naturally occurring resource that may yield further materials with superior electrochemical performance. Furthermore, as the fungal quinones share common biosynthetic pathway traits, it will be possible to use genetic engineering approaches to enhance the production yields and modify quinone structures. By combining these elements, we, therefore, believe that biologically produced quinones may become a real competitor to the currently available synthetic quinones.

Experimental Section

Materials. Potassium hydroxide and sodium sulfate were purchased from MERCK, potassium hexacyanoferrate(II) and potassium hexacyanoferrate(III) were purchased from VWR Chemicals, and sulphuric acid was purchased from Supelco. The chemicals were used as received. Chemicals and reagents for the production of phoenicin were received from suppliers: spore suspension mixture for the fungal strain and cultivation contained 0.5 g L^{-1} Tween 80 (MERCK, 822187) and 0.5 g L^{-1} agar (Bie & Berntsen, BBB 100030, SO-BI-Gel, Agard-Agar), PDA contains 39.0 g L^{-1} Potato Dextrose Agar (DIFCO, 0013-17-6) and 1 mL L^{-1} trace metal solution (10 g L^{-1} $ZnSO_4 \cdot 7H_2O$ (MERCK, 8883); 5 g L^{-1} $CuSO_4 \cdot 5H_2O$). Modified Czapek-yeast-broth growth media contains 5 g L^{-1} yeast extract (Biokar, A1202 HA), 35 g L^{-1} Czapek Dox broth (Difco 233810), 20 ml L^{-1} mineral mix (0.4 g L^{-1} $CuSO_4 \cdot 5H_2O$; 0.8 g L^{-1} $FeSO_4 \cdot 7H_2O$; 8.0 g L^{-1} $ZnSO_4 \cdot 7H_2O$; 0.8 g L^{-1} $MnSO_4 \cdot 2H_2O$; 0.04 g L^{-1} $Na_2B_4O_7 \cdot 10H_2O$; 0.8 g L^{-1} $Na_2MoO_4 \cdot 2H_2O$) and 60 g L^{-1} sucrose (Sigma Aldrich 84100-1 kg). All solutions and media were autoclaved for 20 minutes at 121 °C before use.

Fungal strain and cultivation. *Penicillium atrosanguineum* (IBT 34669), from the IBT culture collection at DTU Bioengineering, was used for the production of phoenicin. The strain was cultivated using 3-point inoculation on 10 plates of Potato Dextrose Agar for 12 days at 25 °C in darkness. A spore suspension was prepared and the number of spores was counted to be 2.625×10^7 spores per mL using a hemocytometer (Thoma). 300 µL from the spore suspension was transferred to 1 L sterilized Ehrlenmeyer flasks with 100 mL modified Czapek-yeast-broth growth media. 20 flasks were inoculated and incubated stationary for 14 days at 25 °C in darkness.

Extraction, identification, and purification of phoenicin. The fungus developed a thick mycelium on top of the growth media, and the supernatant turned dark red/violet during incubation (Figure S15). The supernatant from all flasks was pooled and filtered through a cellulose membrane (Whatman, grade 4, cat. No. 1004-185) and acidified to pH 2 with trifluoroacetic acid (TFA) (Merck, T6508). Phoenicin was extracted with a three-step liquid: liquid partitioning. In the first step, the acidified, filtered supernatant was extracted twice with an equal volume of ethyl acetate (EtOAc) (VWR, 83621.320) and the combined organic phases were

evaporated to dryness. In the second step, the dried extract was re-dissolved in 400 mL EtAOc and partitioned four times with 200 mL and one time with 100 mL sodium hydrogen carbonate water (5 g L^{-1}, MERCK, 1.06329.0500). Because of the slightly alkaline pH, the majority of phoenicin was transferred to the water phases, which were then combined and acidified to pH 2 with TFA. In the third step, the acidified water phase was extracted twice with equal volumes of EtOAc. After the third extraction step, the organic phase was evaporated, re-dissolved, transferred to a Falcon tube, and evaporated under a steam of nitrogen before being freeze-dried to complete dryness.

Phoenicin was identified by tandem MS comparison to a phoenicin standard from an in-house metabolite spectral library across three collision energies of 10, 20, and 40 eV. For each energy, a reverse and a forward score were calculated with Agilent MassHunter PCDL manager software (Agilent Technologies). The scoring is further described in the literature.[65] The scoring as well as the spectra are illustrated in Figure S3.

^{1}H and ^{13}C NMR spectra were recorded on a Bruker Avance 800 MHz spectrometer (Bruker, Billerica, MA, USA). NMR spectra were acquired using standard pulse sequences. The solvent used was DMSO-d_6 and residual solvent peaks at $\delta_H = 2.50$ ppm and $\delta_C = 39.52$ ppm were used as references. The data was processed and analyzed using TopSpin 4.0.7 (Bruker). J-couplings are reported in hertz (Hz) and chemical shifts in ppm (δ). The spectra recorded agrees with the ones found in the litterature.[66]

The purity of phoenicin was investigated by taking a 1 mL sample of the resulting EtOAc phase, evaporating the solvent under a steam of nitrogen, followed by re-dissolving the extract in 1 mL methanol (VWR, 85681.320), and centrifugation. Subsequently, 500 µL was transferred to an HPLC vial and 0.1 µL was injected on an Agilent Infinity 1290 UHPLC-DAD coupled to an Agilent 6545 QTOF-MS. Specific parameters and the method used are described in the literature.[67] The resulting extract contained 1.24 g L^{-1} liquid media with a purity above 95% phoenicin. The 95% was determined by integrating all peaks in the base peak chromatogram in positive electrospray ionization mode (+ESI) and the total wavelength chromatogram generate by the diode array detector (DAD) after HPLC analysis. The area of the phoenicin peak constituted >95% of the intensity observed in both the chromatograms seen in Figure S6. The peaks that were also observed in a solvent blank sample were not integrated.

Protoplast formation. *P. atrosanguineum* was inoculated in 125 mL YES growth medium,[68] and grown in dark at 25 °C for two days at 150 r.p.m. The mycelium was harvested by centrifugation and washed twice with 50 mL KC buffer (60 g L^{-1} KCl (VWR) and 2 g L^{-1} citric acid (VWR), pH 6.2). Protoplast formation was facilitated by resuspending the mycelium in 1 mL KC buffer and incubated with VinoTaste® Pro (Novozymes), Lysing Enzymes from *Trichoderma harzianum* (Sigma-Aldrich), and Chitinase from *Trichoderma viride* (Sigma-Aldrich) to a final concentration of 65 mg mL^{-1}, 22 mg mL^{-1}, and 0.1 mg mL^{-1}, respectively. Cell wall degradation was performed at 37 °C for 30 minutes at 120 r.p.m. followed by stationary incubation at 30 °C for two hours. The protoplast suspension was cooled on ice for 5 minutes followed by filtration in a miracloth. The protoplast was harvested by centrifuging at 600×g for 5 minutes at 4 °C. The pellet was resuspended in 25 mL KC buffer, 25 mL STC buffer (5.5 g L^{-1} calcium chloride dehydrate (Sigma-Aldrich), 219 g L^{-1} sorbitol (VWR), and 10 mL 1 M Tris-HCl buffer, pH of 7.5). The mixture was centrifuged at 600×g for 5 minutes at 4 °C and washed twice with STC buffer.

CRISPR genome editing with protoplast transformation. The donor DNA containing the resistance gene (*hph*) and 1 kb border regions from each direction of the cutting site was synthesized and inserted into a pUC19 vector (GenScript). Donor DNA was amplified using the forward primer 5′-GGCAGAAGCCTTATTTACACC-3′ and reverse primer 5′-TTGTCGTCTTGGGATTCGG-3′. The PCR reaction was performed in 50 µL volume with Phusion polymerase (ThermoFisher Scientific) according to a recommendation of the manufacturer. The lyophilized crRNA (AGTCCTGAAGATCAATGTCATGG) and tracrRNA oligo (IDT) was resuspended in Nuclease-Free Duplex Buffer (IDT) to a stock concentration of 1.0×10^{-4} M. The sgRNA complex was prepared by mixing tracrRNA with crRNA and Nuclease-Free Duplex Buffer in equimolar concentrations. The solution was heated to 95 °C for 5 minutes and then cooled at room temperature for 15 minutes. Alt-R® S.p. Cas9 Nuclease V3 (10 µg μL^{-1}) (IDT) was diluted 1:10 with sterilized Cas9 activity buffer (2.0×10^{-2} m) HEPES (Sigma-Aldrich) pH 7.5, 0.15×10^{-3} M KCl (VWR), 5.0×10^{-4} M DTT (ThermoFisher Scientific), 1.0×10^{-4} M EDTA (Fermentas), 1.0×10^{-2} M $MgCl_2$ (ThermoFisher Scientific). The RNP complex was prepared by mixing 1.5 µL sgRNA complex solution with 0.75 µL of diluted Alt-R® S.p. Cas9 Nuclease V3 (IDT) and 11 µL Cas9 activity buffer. The mixture was incubated at room temperature for 5 minutes to assemble the RNA complex. 200 µL of the protoplast solution was added together with 1 µg donor DNA and 25 µL 60% PEG 4000 (Sigma-Aldrich) and incubated on ice for 50 minutes. Subsequently, 1.25 mL 60% PEG 4000 (Sigma-Aldrich) was added and another incubation step at room temperature for 20 minutes was performed to allow the uptake of RNAs and donor DNA into the protoplasts. The Falcon tube was filled up to 3 mL with autoclaved 2xSTC buffer (10 g L^{-1} calcium chloride dehydrate (Sigma-Aldrich), 438 g L^{-1} sorbitol (VWR), 20 mL 1 M Tris-HCl buffer with a pH of 7.5). The mixture was plated on osmotic recovery plates (20 g L^{-1} yeast extract (ThermoFisher), 75 g L^{-1} sucrose (VWR), 0.5 g L^{-1} $MgSO_4\cdot7H_2O$ (Sigma-Aldrich), 0.016 g L^{-1} $ZnSO_4\cdot7H_2O$ (Sigma-Aldrich), 0.005 g L^{-1} $CuSO_4\cdot7H_2O$ (Sigma-Aldrich), 20 g L^{-1} agar (VWR), and 1 M sorbitol (VWR)).

Confirmation of KO mutant. Correct integration of the knockout cassette was initially verified by diagnostic PCR followed by full genome sequencing as previously described.[69]

UV-vis calibration curve preparation. To detect the actual concentration of phoenicin in the samples used for the electrochemical analysis, an absorbance-calibration curve was made using UV-vis (Cary 50 Spectrophotometer). Samples of known concentration were scanned from 1,000 to 200 nm and the absorbance was measured (Figure S7a). The best line fit was made for the wavelength of 525 nm (Figure S7b). Before the scans were made, a background scan of 1 M KOH supportive electrolyte was measured as a baseline.

Electrochemical analysis. Cyclic voltammetry and rotating disc electrode (RDE) measurements were conducted using a µAutolabIII/FRA2 potentiostat/galvanostat (Methrom Autolab) and NOVA 2.1 software. The measurements were performed using a three-electrode set-up consisting of a glassy carbon disk (3 mm diameter) as the working electrode (polished for one minute with aluminum oxide powder mixed with distilled water on a polishing cloth (Polishing set, Methrom) before measurements), Ag/AgCl in 3 M NaCl solution as the reference electrode (+0.213 V *vs.* SHE[5,64]), and platinum wire as the counter electrode. All the electrodes were obtained from Methrom Autolab. The CV measurements of phoenicin and $K_4Fe(CN)_6$ were collected using a scan rate of 10 mV s^{-1} unless otherwise stated. The solution was degassed with nitrogen for 30 minutes before all CV and RDE measurements.

For Randles-Sevcik analysis, the potential was negatively swept from 0 to −1.3 V *vs.* Ag/AgCl, with a potential hold at 0 V for 1 minute before each sweep. Background scans measured under the same conditions in blank 1 M KOH supportive electrolyte were

subtracted during the data treatment. The concentration of the samples was evaluated by UV-vis at 525 nm before and after the Randles-Sevcik analysis. An average of the phoenicin concentrations estimated by UV-vis was used in further evaluation to calculate the diffusion coefficient.

The rotation rate for the RDE experiments was controlled externally by an Autolab RDE motor controller (Methrom Autolab). 3.0×10^{-3} M phoenicin in 1 M KOH solution was used for the analysis. The potential of the rotating glassy carbon disk electrode (3 mm diameter) was kept for 1 minute at 0 V *vs.* Ag/AgCl and then negatively swept to −1.3 V using a sweep rate of 5 mV s^{-1}. The RDE was rotated at rates between 100–2,500 r.p.m. starting from high to low. Four separate experiments were made and currents for each rotation rate measured in each separate experiment were averaged. Background scans measured under the same conditions in blank 1 M KOH supportive electrolyte were subtracted. Limiting currents for the Levich plot were measured as the average current of the potential range from −1.0 to −1.1 V *vs.* Ag/AgCl. The concentration of the samples was evaluated by UV-vis at 525 nm before and after the RDE measurements (Figure S9a). An average estimated concentration of 2.64×10^{-3} M (C^*_0) was used to further evaluate the diffusion and kinetic parameters. The RDE results were analyzed via Levich plot (limiting current i_{lim} *vs.* $\omega^{1/2}$) from which we determined D using the Levich equation $i_{lim}=0.62nFAD^{2/3}\omega^{1/2}v^{-1/6}C^*_0$, where n is the number of transferred electrons (2), F is the Faraday's constant (96485 C mol^{-1}), A is the electrode surface area (0.0707 cm^2), and v is the kinematic viscosity (0.01 cm^2 s^{-1}[5,43]).[70] We used the Koutecky-Levich plot to analyze the currents for overpotentials (between −30 and −100 mV) in order to prepare the Tafel plot, where we have made a linear fit to the experimental data using the Butler-Volmer model.[71] As there were no reduced species in the bulk, we have assumed the oxidation-related part of the Butler-Volmer equation negligible, thus, the transformed equation, which describes the current-overpotential relation is presented as follows: $i=nFAk^0\,[C^*_{Ox}\,exp(-\alpha F(E-E^{0'})/RT)]$ or $log_{10}(i)=-2.3\alpha F(E-E^{0'})/RT+log_{10}(FAk^0C^*_0)$, where R is the universal gas constant and T is the temperature, and $E-E^{0'}$ is the overpotential. Subsequently, from the linear fit to the Tafel plot, we used the slope to determine α with: $slope=-\alpha F/(2.3RT)$, and we used the intercept to determine k^0 with: $intercept=log_{10}(FAk^0C^*_0)$.

At the end of the RDE experiment, an additional LSV sweep was made at 2,500 r.p.m., to assess end currents, i(end), and to further compare them with currents measured at the beginning of the RDE experiment, i(start) (Figure S9b). The absolute values of i(end) are smaller compared to i(start), hinting that there occurs decomposition or structural reorganization of phoenicin. Such processes may cause RDE passivation and consequent data inaccuracies. Nevertheless, the i(end) values normalized by the share of initial and final phoenicin concentrations, measured by UV-vis before and after the RDE experiment, are very similar to the i(start) (Figure S9b), confirming that no working electrode passivation takes place. Thus, even though phoenicin decomposes or is structurally reorganized during the measurement, replacement of the preparation concentration value with the average value of the UV-vis estimated initial and final concentrations helps to exclude inaccuracies coming from the degradation of the negolyte.

Cell assembly. The symmetric cell cycling test and the full cell cycling test were performed using a single lab-scale RFB test cell (JenaBatteries GmbH, Jena, Germany) with a membrane and electrode active area of 5 cm^2, as published elsewhere.[70] Each side of the cell contained a poly(tetrafluoroethylene) (PTFE) frame, rubber seals, and porous graphite felt electrodes ($2.25\times2.25\times0.4$ cm^3, GFA6, SGL Carbon) compressed between graphite current collectors. The cells were assembled with a Nafion 117 cation exchange membrane (FuelCellStore) as the separator. The battery tests were carried out using a VMP3 potentiostat/galvanostat (BioLogic, France). Before cell cycling in the experiments, the resistance of the setup was measured by potentiostatic electrochemical impedance spectroscopy (Figure S11b, d).

In the symmetric cell cycling test, a peristaltic pump (Pumpdrive 5001, Heidolph) was used to circulate the electrolyte through the cell and the storage tanks at a flow rate of 60 r.p.m., through Tygon tubes (inner diameter: 1.6 mm). In the full cell cycling test, two diaphragm dosing pumps (FEM 1.09 SM-2 TT, KNF) were used for electrolyte circulation with a nominal flow rate of 50 mL min^{-1} through PTFE tubes.

Symmetric cell cycling. For the symmetric cell cycling test a volumetrically unbalanced, compositionally symmetric flow cell method was used.[62] The working electrode was connected to a capacity limiting side (CLS) which contained a solution of 50% SOC 0.1 M phoenicin in 10 mL 2.1 M KOH. As the negative reservoir, a non-capacity limiting side (NCLS) contained a solution of 50% SOC 0.1 M phoenicin in 20 mL 2.1 M KOH. To prepare a 50% SOC electrolyte, a portion of freshly mixed uncharged 0.1 M phoenicin in 2.1 M KOH was charged against potassium ferrocyanide in a full cell. The full cell was charged galvanostatically at 0.4 A with potentiostatic hold at 1.6 V until the current decayed below 2.5 mA (0.5 mA cm^{-2}), whereas the electrolyte was assumed to be fully charged. The fully charged phoenicin solution was mixed with an equal amount of uncharged 0.1 M phoenicin solution to obtain the 50% SOC electrolyte. The symmetric cell cycling test was performed in an argon-filled glovebox at room temperature. Potentiostatic cell cycling with potential limits of ±300 mV was performed continuously for 1.7 days, then 24 h pauses at various fixed SOCs were implemented. During the pauses, the pumping was stopped. Ten charge and discharge cycles were performed between each of the pauses and after the last one. The difference between discharge capacity averaged over ten cycles from values before and after each pause was used to measure the decay for each of the fixed SOCs. All electrolyte solutions were degassed with argon before bringing into the glovebox.

Full cell cycling. For the full cell cycling test, phoenicin was exploited as the negolyte against ferrocyanide as the posolyte. The electrolytes consisted of 0.2 M phoenicin in 20 mL of 2.1 M KOH negolyte and 0.16 M $K_4Fe(CN)_6$/0.04 M $K_3Fe(CN)_6$ in 60 mL of 1 M KOH posolyte. The experiment was performed at room temperature in a nitrogen-filled glove bag with a continuous flow of nitrogen. The negolyte and the posolyte were degassed with argon. The battery was charged galvanostatically at 0.4 A with potentiostatic holds at 1.6 V when charging and at 0.6 V when discharging until the current decayed below 2.5 mA (0.5 mA cm^{-2}).

IR spectroscopy. In situ infrared (IR) spectra were recorded using a liquid nitrogen-cooled ReactIR 701 L (Mettler Toledo, Germany), equipped with a Micro Flow Cell DS DIComp (Mettler Toledo, Germany) between 650 and 4,000 cm^{-1} at a resolution of 4 cm^{-1} using a diamond ATR crystal. A background spectrum of 2.1 M KOH solution in deionized water was collected with 128 single scans prior to the experiment. Each individual *in situ* IR spectrum consists of 138 single scans, which corresponds to a measurement time of 90 s per spectrum. To account for the baseline effects, the IR spectrum was pre-processed using Multiplicative Scatter Correction (MSC) (Figure S14).

Acknowledgements

We acknowledge the funding from The Danish Research Council, Technology and Production (Grant No. 7017-00167) and the Novo Nordisk Foundation (NNF18OC0034952) to support this study.

Conflict of Interest

The authors declare no conflict of interest.

Data Availability Statement

The data that support the findings of this study are available from the corresponding author upon reasonable request.

Keywords: aqueous redox flow batteries · energy storage · filamentous fungi · natural products · quinones

[1] W. Chen, G. Li, A. Pei, Y. Li, L. Liao, H. Wang, J. Wan, Z. Liang, G. Chen, H. Zhang, J. Wang, Y. Cui, *Nat. Energy* **2018**, *3*, 428.
[2] U. S. Energy Information Administration, *International Energy Outlook 2019*, Washington, DC, **2019**.
[3] P. Sun, Y. Liu, Y. Li, M. A. Shehzad, Y. Liu, P. Zuo, Q. Chen, Z. Yang, T. Xu, *Ind. Eng. Chem. Res.* **2019**, *58*, 3994–3999.
[4] M. Park, J. Ryu, W. Wang, J. Cho, *Nat. Rev. Mater.* **2017**, *2*, 16080.
[5] Z. Yang, L. Tong, D. P. Tabor, E. S. Beh, M.-A. Goulet, D. De Porcellinis, A. Aspuru-Guzik, R. G. Gordon, M. J. Aziz, *Adv. Energy Mater.* **2018**, *8*, 1702056.
[6] B. Hu, C. Debruler, Z. Rhodes, T. L. Liu, *J. Am. Chem. Soc.* **2017**, *139*, 1207–1214.
[7] L. F. Arenas, C. Ponce de León, F. C. Walsh, *J. Energy Storage* **2017**, *11*, 119–153.
[8] K. Lin, R. Gómez-Bombarelli, E. S. Beh, L. Tong, Q. Chen, A. Valle, A. Aspuru-Guzik, M. J. Aziz, R. G. Gordon, *Nat. Energy* **2016**, *1*, 16102.
[9] Y. Huo, X. Xing, C. Zhang, X. Wang, Y. Li, *RSC Adv.* **2019**, *9*, 13128–13132.
[10] A. Khataee, J. Azevedo, P. Dias, D. Ivanou, E. Dražević, A. Bentien, A. Mendes, *Nano Energy* **2019**, *62*, 832–843.
[11] T. M. Gür, *Energy Environ. Sci.* **2018**, *11*, 2696–2767.
[12] X. Ke, J. M. Prahl, J. I. D. Alexander, J. S. Wainright, T. A. Zawodzinski, R. F. Savinell, *Chem. Soc. Rev.* **2018**, *47*, 8721–8743.
[13] Y. Yao, J. Lei, Y. Shi, F. Ai, Y.-C. Lu, *Nat. Energy* **2021**, *6*, 582–588.
[14] P. Navalpotro, J. Palma, M. Anderson, R. Marcilla, *Angew. Chem. Int. Ed.* **2017**, *56*, 12460–12465; *Angew. Chem.* **2017**, *129*, 12634–12639.
[15] P. Alotto, M. Guarnieri, F. Moro, *Renewable Sustainable Energy Rev.* **2014**, *29*, 325–335.
[16] R. Chen, *ChemElectroChem* **2019**, *6*, 603–612.
[17] I. Gyuk, M. Johnson, J. Vetrano, K. Lynn, W. Parks, R. Handa, L. Kannberg, S. Hearne, K. Waldrip, R. Braccio, "Grid Energy Storage. U. S. Department of Energy", can be found under https://www.energy.gov/sites/prod/files/2014/09/f18/Grid%20Energy%20Storage%20December%202013.pdf, **2013** (accessed 27 October 2022).
[18] Y. Ding, Y. Li, G. Yu, *Chem* **2016**, *1*, 790–801.
[19] Y. Jing, M. Wu, A. A. Wong, E. M. Fell, S. Jin, D. A. Pollack, E. F. Kerr, R. G. Gordon, M. J. Aziz, *Green Chem.* **2020**, *22*, 6084–6092.
[20] D. G. Kwabi, K. Lin, Y. Ji, E. F. Kerr, M.-A. Goulet, D. De Porcellinis, D. P. Tabor, D. A. Pollack, A. Aspuru-Guzik, R. G. Gordon, M. J. Aziz, *Joule* **2018**, *2*, 1894–1906.
[21] L. Xia, Y. Zhang, H. Zhang, S. Jiang, Q. Lv, W. Huo, F. Chu, F. Wang, H. Li, Z. Tan, *Sustain. Energy Fuels* **2022**, *6*, 2045–2052.
[22] Y. Zhu, Y. Li, Y. Qian, L. Zhang, J. Ye, X. Zhang, Y. Zhao, *J. Power Sources* **2021**, *501*, 229984.
[23] W. Lee, A. Permatasari, Y. Kwon, *J. Mater. Chem. C* **2020**, *8*, 5727–5731.
[24] F. Chu, M. Su, G. Xiao, Z. Tan, G. Yang, *Ind. Eng. Chem. Res.* **2022**, *61*, 2915–2925.
[25] R. B. Jethwa, E. W. Zhao, R. N. Kerber, E. Jónsson, D. S. Wright, C. P. Grey, *J. Mater. Chem. A* **2021**, *9*, 15188–15198.
[26] J. Rubio-Garcia, A. Kucernak, A. Parra-Puerto, R. Liu, B. Chakrabarti, *J. Mater. Chem. A* **2020**, *8*, 3933–3941.
[27] W. Lee, G. Park, D. Schröder, Y. Kwon, *Korean J. Chem. Eng.* **2022**, *39*, 1624–1631.
[28] G. Park, W. Lee, Y. Kwon, *Int. J. Energy Res.* **2022**, *46*, 3362–3375.
[29] E. S. Beh, D. De Porcellinis, R. L. Gracia, K. T. Xia, R. G. Gordon, M. J. Aziz, *ACS Energy Lett.* **2017**, *2*, 639–644.
[30] W. Wu, J. Luo, F. Wang, B. Yuan, T. L. Liu, *ACS Energy Lett.* **2021**, *6*, 2891–2897.
[31] H. Li, H. Fan, B. Hu, L. Hu, G. Chang, J. Song, *Angew. Chem. Int. Ed.* **2021**, *60*, 26971–26977.
[32] A. Korshunov, A. Gibalova, M. Gruenebaum, B. J. Ravoo, M. Winter, I. Cekic-Laskovic, *ACS Appl. Energ. Mater.* **2021**, *4*, 12353–12364.
[33] Y. Liu, M.-A. Goulet, L. Tong, Y. Liu, Y. Li, L. Wu, R. G. Gordon, M. J. Aziz, Z. Yang, T. Xu, *Chem* **2019**, *5*, 1861–1870.
[34] M. Pan, L. Gao, J. Liang, P. Zhang, S. Lu, Y. Lu, J. Ma, Z. Jin, *Adv. Energy Mater.* **2022**, *12*.
[35] O. Nolte, P. Rohland, N. Ueberschaar, M. D. Hager, U. S. Schubert, *J. Power Sources* **2022**, *525*, 230996.
[36] B. Hu, M. Hu, J. Luo, T. L. Liu, *Adv. Energy Mater.* **2022**, *12*, 1–5.
[37] P. S. Borchers, M. Strumpf, C. Friebe, I. Nischang, M. D. Hager, J. Elbert, U. S. Schubert, *Adv. Energy Mater.* **2020**, *10*, 2001825.
[38] J. Winsberg, T. Hagemann, T. Janoschka, M. D. Hager, U. S. Schubert, *Angew. Chem. Int. Ed.* **2017**, *56*, 686–711; *Angew. Chem.* **2017**, *129*, 702–729.
[39] J. Luo, B. Hu, M. Hu, Y. Zhao, T. L. Liu, *ACS Energy Lett.* **2019**, *4*, 2220–2240.
[40] E. Sánchez-Díez, E. Ventosa, M. Guarnieri, A. Trovò, C. Flox, R. Marcilla, F. Soavi, P. Mazur, E. Aranzabe, R. Ferret, *J. Power Sources* **2021**, *481*, 228804.
[41] H. Bui, N. E. Holubowitch, *Int. J. Energy Res.* **2022**, *46*, 5864–5875.
[42] B. R. Chalamala, T. Soundappan, G. R. Fisher, M. R. Anstey, V. V. Viswanathan, M. L. Perry, *Proc. IEEE* **2014**, *102*, 976–999.
[43] C. Wang, Z. Yang, Y. Wang, P. Zhao, W. Yan, G. Zhu, L. Ma, B. Yu, L. Wang, H. Li, J. Liu, Z. Jin, *ACS Energy Lett.* **2018**, *3*, 2404–2409.
[44] W. Schlemmer, P. Nothdurft, A. Petzold, G. Riess, P. Frühwirt, M. Schmallegger, G. Gescheidt-Demner, R. Fischer, S. A. Freunberger, W. Kern, S. Spirk, *Angew. Chem. Int. Ed.* **2020**, *59*, 22943–22946; *Angew. Chem.* **2020**, *132*, 23143–23146.
[45] A. Orita, M. G. Verde, M. Sakai, Y. S. Meng, *Nat. Commun.* **2016**, *7*, 13230.
[46] S. A. Petrova, M. V. Kolodyazhny, O. S. Ksenzhek, *J. Electroanal. Chem.* **1990**, *277*, 189–196.
[47] P. S. Guin, S. Das, P. C. Mandal, *Int. J. Electrochem.* **2011**, *2011*, 816202.
[48] M. Quan, D. Sanchez, M. F. Wasylkiw, D. K. Smith, *J. Am. Chem. Soc.* **2007**, *129*, 12847–12856.
[49] K. Eljounaidi, B. R. Lichman, *Front. Chem.* **2020**, *8*, 596479.
[50] R. Breitling, E. Takano, *Curr. Opin. Biotechnol.* **2015**, *35*, 46–51.
[51] S. B. Kristensen, T. van Mourik, T. B. Pedersen, J. L. Sørensen, J. Muff, *Sci. Rep.* **2020**, *10*, 13571.
[52] E. A. H. Friedheim, *C. R. Soc. Biol.* **1933**, *112*, 1030–1032.
[53] D. Ebene, E. Steiner, E. Charollais, T. Posternak, *Helv. Chem. Acta* **1974**, *57*, 2368–2376.
[54] T. Posternak, *Helv. Chem. Acta* **1938**, *21*, 1326–1337.
[55] E. Steiner, J. Kalamar, E. Charollais, T. Posternak, *Helv. Chem. Acta* **1974**, *57*, 2377–2387.
[56] J. V. Christiansen, T. Isbrandt, R. Asferg, S. A. Jarmusch, T. O. Larsen, J. C. Frisvad, *Appl. Environ. Microbiol.* **2022**, *88*.
[57] P. Feng, Y. Shang, K. Cen, C. Wang, *Proc. Natl. Acad. Sci. USA* **2015**, *112*, 11365–11370.
[58] H. Musso, H.-G. Matthies, *Chem. Ber.* **1961**, *94*, 356–368.
[59] N. Aristov, A. Habekost, *World J. Chem. Educ.* **2015**, *3*, 115–119.
[60] D. G. Kwabi, Y. Ji, M. J. Aziz, *Chem. Rev.* **2020**, *120*, 6467–6489.
[61] O. Nolte, I. A. Volodin, C. Stolze, M. D. Hager, U. S. Schubert, *Mater. Horiz.* **2021**, *8*, 1866–1925.
[62] M. Goulet, M. J. Aziz, *J. Electrochem. Soc.* **2018**, *165*, A1466–A1477.
[63] R. Gulaboski, I. Bogeski, V. Mirčeski, S. Saul, B. Pasieka, H. H. Haeri, M. Stefova, J. P. Stanoeva, S. Mitrev, M. Hoth, R. Kappl, *Sci. Rep.* **2013**, *3*, 1865.
[64] K. Lin, Q. Chen, M. R. Gerhardt, L. Tong, S. B. Kim, L. Eisenach, A. W. Valle, D. Hardee, R. G. Gordon, M. J. Aziz, Marshak, *Science* **2015**, *349*, 1529–1532.

[65] S. Kildgaard, M. Mansson, I. Dosen, A. Klitgaard, J. C. Frisvad, T. O. Larsen, K. F. Nielsen, *Mar. Drugs* **2014**, *12*, 3681–3705.
[66] B. E. Love, J. Bonner-Stewart, L. A. Forrest, *Tetrahedron Lett.* **2009**, *50*, 5050–5052.
[67] K. Subko, S. Kildgaard, F. Vicente, F. Reyes, O. Genilloud, T. O. Larsen, *Mar. Drugs* **2021**, *19*, 46.
[68] J. L. Sørensen, T. E. Sondergaard, *Int. J. Food Microbiol.* **2014**, *170*, 55–60.
[69] K. R. Westphal, K. A. H. Nielsen, S. Bachleitner, L. Studt, E. Lysøe, H. Giese, R. Wimmer, J. L. Sørensen, T. E. Sondergaard, *Toxins* **2019**, *11*, 277.
[70] T. Janoschka, N. Martin, U. Martin, C. Friebe, S. Morgenstern, H. Hiller, M. D. Hager, U. S. Schubert, *Nature* **2015**, *527*, 78–81.
[71] A. J. Bard, L. R. Faulkner, *Electrochemical Methods – Fundamentals and Applications*, John Wiley & Sons, inc., USA, 2nd edn, **2001**, pp. 87–132.

Manuscript received: August 18, 2022
Revised manuscript received: October 7, 2022
Accepted manuscript online: October 10, 2022
Version of record online: November 3, 2022